

# Effects of strong fringing magnetic fields on turbulent thermal convection

Shashwat Bhattacharya<sup>1</sup>†, Thomas Boeck<sup>1</sup>, Dmitry Krasnov<sup>1</sup> and Jörg Schumacher<sup>1,2</sup>

<sup>1</sup>Institute of Thermodynamics and Fluid Mechanics, Technische Universität Ilmenau, Postfach 100565, D-98684 Ilmenau, Germany

<sup>2</sup>Tandon School of Engineering, New York University, New York 11021, USA

(Received xx; revised xx; accepted xx)

We study the influence of fringing magnetic fields on turbulent thermal convection in a horizontally extended rectangular domain. The magnetic field is created in the gap between two semi-infinite planar magnetic poles, with the convection layer located near the edge of the gap. We employ direct numerical simulations in this setup for fixed Rayleigh and small Prandtl numbers, but vary the fringe-width by controlling the gap between the magnetic poles and the convection cell. The magnetic field generated by the magnets is strong enough to cease the flow in high magnetic flux region of the convection cell. We observe that as the local vertical magnetic field strength increases, the large scale structures become thinner and align themselves perpendicular to the longitudinal sidewalls. We determine the local Nusselt and Reynolds numbers as functions of the local Hartmann number (based on the vertical component of the magnetic field) and estimate the global heat and momentum transport. We show that the global heat transport decreases with increasing fringe-width for strong magnetic fields but decreases with increasing fringe-width for weak magnetic fields. In the regions of large vertical magnetic fields, the convective motion becomes confined to the vicinity of the sidewalls. The amplitudes of these wall modes show a non-monotonic dependence on the fringe-width.

## 1. Introduction

Flows that are driven by buoyancy forces are a common occurrence in nature as well as in technological applications. The driving mechanism is the temperature dependence of the fluid density, which leads to density variations when heat is transported through the fluid. A simplified paradigm for such flows is the Rayleigh-Bénard convection (RBC), which consists of a fluid layer that is heated from below and cooled from above (Chandrasekhar 1981). While the understanding of RBC has increased substantially in the past decades (see, for example, Ahlers *et al.* 2009; Chillà & Schumacher 2012; Verma 2018), it must be noted that a multitude of additional forces, such as those generated by rotation and magnetic fields, can affect buoyancy-driven convection in nature or in industrial applications. The effects of these forces have been relatively less explored. The present study deals with magnetoconvection, that is, thermal convection of electrically conducting fluids under the effect of magnetic fields.

In magnetoconvection, flows are acted upon by buoyancy as well as by Lorentz forces generated due to a magnetic field (Weiss & Proctor 2014). Convection in the Sun and planetary dynamos are examples of magnetoconvection occurring in nature where the

† Email address for correspondence: shashwat.bhattacharya@tu-ilmenau.de

magnetic field is maintained by the flow. In technological applications the magnetic field is usually not primarily caused by the flow but externally imposed. Examples are liquid metal batteries for renewable energy storage, growth of semiconductor monocrystals, flow control of hot metal melts by electromagnetic brakes in metallurgy, and heat transfer in blankets in nuclear fusion reactors.

Magnetoconvection is governed by the equations for conservation of mass, momentum and energy as well as Maxwell's equations and Ohm's law. The governing nondimensional parameters of magnetoconvection are i) Rayleigh number  $Ra$  – the ratio of buoyancy to dissipative forces, ii) Prandtl number  $Pr$  – the ratio of kinematic viscosity to thermal diffusivity, iii) Hartmann number  $Ha$  – the ratio of Lorentz to viscous force, and iv) the magnetic Prandtl number  $Pm$  – the ratio of kinematic viscosity to magnetic diffusivity. The important nondimensional output parameters of magnetoconvection are i) the Nusselt number  $Nu$ , which quantifies the global heat transport, ii) the Reynolds number  $Re$  – the ratio of inertial forces to viscous forces, and iii) the magnetic Reynolds number  $Rm$  – the ratio of induction to diffusion of the magnetic field. For sufficiently small magnetic Reynolds numbers, the induced magnetic field is negligible compared to the applied magnetic field and is therefore neglected in the expressions of Lorentz force and Ohm's law (Roberts 1967; Davidson 2017; Verma 2019). In such cases, referred to as quasi-static magnetoconvection, the induced magnetic field adjusts instantaneously to the changes in velocity. In the *quasi-static approximation*, there exists a one-way influence of the magnetic field on the flow only.

Magnetoconvection has been studied theoretically in the past (for example, Chandrasekhar 1981; Houchens *et al.* 2002; Busse 2008) as well as with the help of experiments (for example, Nakagawa 1957; Fauve *et al.* 1981; Cioni *et al.* 2000; Aurnou & Olson 2001; Burr & Müller 2001; King & Aurnou 2015; Vogt *et al.* 2018, 2021; Zürner *et al.* 2020; Grannan *et al.* 2022) and numerical simulations (for example, Liu *et al.* 2018; Yan *et al.* 2019; Akhmedagaev *et al.* 2020a,b; Nicoski *et al.* 2022). A horizontal magnetic field has been found to cause the large-scale rolls to become quasi two-dimensional and align in the direction of the field (Fauve *et al.* 1981; Busse & Clever 1983; Burr & Müller 2002; Yanagisawa *et al.* 2013; Tasaka *et al.* 2016; Vogt *et al.* 2018, 2021). These self-organized flow structures reach an optimal state characterised by a significant increase in heat transport and convective velocities (Vogt *et al.* 2021). In contrast, strong vertical magnetic fields suppress convection (Chandrasekhar 1981; Cioni *et al.* 2000; Zürner *et al.* 2020; Akhmedagaev *et al.* 2020a,b) with the flow ceasing above a critical Hartmann number. At this threshold, the flow in the center is fully suppressed with convective motion only in the vicinity of sidewalls (Busse 2008; Liu *et al.* 2018; Zürner *et al.* 2020; Akhmedagaev *et al.* 2020a,b) if existent. These so-called wall modes, which are also present in confined rotating convection (Zhong *et al.* 1991; Ecke *et al.* 1992; Goldstein *et al.* 1993, 1994; Liu & Ecke 1999; King *et al.* 2012), are particularly relevant in technical applications in closed vessels. Hurlburt *et al.* (1996) and Nicoski *et al.* (2022) studied convection with tilted magnetic fields. The results of Hurlburt *et al.* (1996) suggest that the mean flows tend to travel in the direction of the tilt. Nicoski *et al.* (2022) reported qualitative similarities between convection with tilted magnetic field and that with vertical magnetic field in terms of the behavior of convection patterns, heat transport, and flow speed. It must be noted that all the aforementioned works on magnetoconvection have been restricted to uniformly imposed magnetic field, which is a highly idealized approximation. However, in experiments and industrial applications, creating a strong and homogeneous magnetic field is practically not possible and hence one always deals with magnetic fields that vary in space (Votyakov *et al.* 2009).

Convection flows in horizontally extended domains are often organized into prominent

and coherent large-scale patterns that persist for very long times and can extend over scales in the lateral direction that are much larger than the domain height. These so-called superstructures have a strong influence on the turbulent transport properties of the flow. A prominent example of such superstructures is the granulation at the surface of the Sun (Schumacher & Sreenivasan 2020). While the understanding of the process of formation and evolution of these superstructures and their characteristic scales in the absence of magnetic fields has improved significantly over the recent years (see, for example, Pandey *et al.* 2018; Stevens *et al.* 2018; Krug *et al.* 2020), the case with inhomogeneous magnetic fields still leaves several questions open as the physical complexity is increased.

In the present work, we attempt to fill some of these gaps and study the effect of strong spatially varying magnetic fields in turbulent convection under the quasi-static approximation. The effects of localized magnetic fields on turbulent superstructures in horizontally extended domains and their impact on the local and global turbulent heat and momentum transport are explored. We consider a Rayleigh-Bénard cell of large aspect ratio with fringing magnetic fields generated by semi-infinite magnetic poles. We study the spatial variation of size and orientation of turbulent superstructures along with the turbulent transport inside the convection cell. We also study wall-attached convection in the regions of strong magnetic flux regions, the wall modes. Although the setup is a simple way to study the influence of spatially varying magnetic fields on convection, it permits us to carry out such a parametric study systematically. This is the main motivation of the present work. Future studies can be conducted in a similar manner for more complex arrangements.

The outline of the paper is as follows. §2 describes the magnetoconvection setup along with the governing equations of magnetoconvection and the spatial distribution of the magnetic field. The details of our numerical simulations are also discussed in §2. In § 3, we present the numerical results, detailing the behavior of large-scale structures, the spatial distribution of heat and momentum transport along with their variations with the magnetic field, the dependence of the global heat and momentum transport on the fringe-width, and wall-attached convection. We conclude in §4 with a summary and an outlook.

## 2. Numerical model

### 2.1. Problem setup and equations

We consider a horizontally extended convection cell of size  $l_x \times l_y \times H$  which is under the influence of a magnetic field generated by two semi-infinite permanent magnets. The north pole of one magnet faces the bottom of the convection cell and the south pole of the second magnet faces the top of the convection cell. These magnets extend from  $-\infty$  to  $\infty$  in the  $x$ -direction,  $l_y/2$  to  $\infty$  in the  $y$ -direction, from near the top wall to  $\infty$  in the positive  $z$ -direction, and from near the bottom wall to  $-\infty$  in the negative  $z$  direction. A schematic of the arrangement is provided in figure 1. Using the model of Votyakov *et al.* (2009) for permanent magnets, we obtain the following relations for the non-dimensional imposed magnetic field  $\mathbf{B}_0 = \{B_x, B_y, B_z\}$  generated in the above configuration:

$$B_x = 0, \quad (2.1)$$

$$B_y = -\ln \left[ \frac{(y - y_c)^2 - \{(z - z_c) - (H/2 + \delta)\}^2}{(y - y_c)^2 + \{(z - z_c) + (H/2 + \delta)\}^2} \right], \quad (2.2)$$

$$B_z = -2 \arctan \left[ \frac{2(H/2 + \delta)(y - y_c)}{(y - y_c)^2 + (z - z_c)^2 - (H/2 + \delta)^2} \right], \quad (2.3)$$

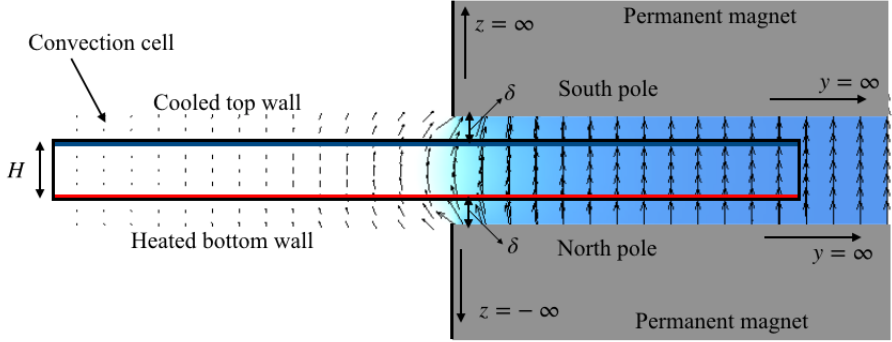


FIGURE 1. Schematic of the proposed magnetoconvection arrangement. The semi-infinite permanent magnets (colored in grey) generate the localized magnetic field represented by the vector plots drawn in the convection cell. The magnetic field distribution is described by equations (2.1) to (2.3).

where  $y_c$  and  $z_c$  are the  $y$  and  $z$  coordinates, respectively, of the cell-center, and  $\delta$  is the gap between the permanent magnet and the top/bottom wall (see figure 1). The aforementioned magnetic field distribution satisfies  $\nabla \times \mathbf{B}_0 = 0$  and  $\nabla \cdot \mathbf{B}_0 = 0$ . In the above configuration, the magnetic field is almost absent in nearly half of the RBC cell (for  $y \lesssim l_y/2$ ), increases steeply about the midplane ( $y \approx l_y/2$ ), and then becomes strong in the other half of the cell (for  $y \gtrsim l_y/2$ ). The region where the gradient of the magnetic field is large is called the fringe zone. The region of the convection cell that is outside the gap between the magnets will be henceforth referred to as *weak magnetic flux region* and the one inside the gap will be referred to as *strong magnetic flux region*.

Equations (2.2) and (2.3) imply that the spatial distribution of the magnetic field is strongly dependent on the gap width ( $\delta$ ) between the magnetic poles and the convection cell. In figures 2(a) and (b), we plot, respectively, the mean vertical and horizontal magnetic field profiles versus the lengthwise coordinate  $y$ . As evident in figure 2(a), the gradient of the vertical magnetic field decreases as  $\delta$  is increased; this implies that the width of the fringe zone increases with an increase in  $\delta$ . Further, the horizontal component of the magnetic field on the lateral vertical midplane at  $y = l_y/2$  increases with a decrease in  $\delta$ . These variations in the magnetic field profile affect the convection patterns along with the associated global heat transport and will be studied in detail in the later sections.

The study will be conducted under the quasi-static approximation, in which the induced magnetic field is neglected as it is very small compared to the applied magnetic field. This approximation is fairly accurate for magnetoconvection in liquid metals (Davidson 2017). The nondimensionalized governing equations are as follows:

$$\nabla \cdot \mathbf{u} = 0 \quad (2.4)$$

$$\frac{\partial \mathbf{u}}{\partial t} + \mathbf{u} \cdot \nabla \mathbf{u} = -\nabla p + T\hat{z} + \sqrt{\frac{Pr}{Ra}} \nabla^2 \mathbf{u} + Ha_{z,max}^2 \sqrt{\frac{Pr}{Ra}} (\mathbf{j} \times \tilde{\mathbf{B}}), \quad (2.5)$$

$$\frac{\partial T}{\partial t} + \mathbf{u} \cdot \nabla T = \frac{1}{\sqrt{RaPr}} \nabla^2 T, \quad (2.6)$$

$$\mathbf{j} = -\nabla \phi + (\mathbf{u} \times \tilde{\mathbf{B}}), \quad (2.7)$$

$$\nabla^2 \phi = \nabla \cdot (\mathbf{u} \times \tilde{\mathbf{B}}), \quad (2.8)$$

where  $\mathbf{u}$ ,  $\mathbf{j}$ ,  $p$ ,  $T$ , and  $\phi$  are the fields of velocity, current density, pressure, temperature,

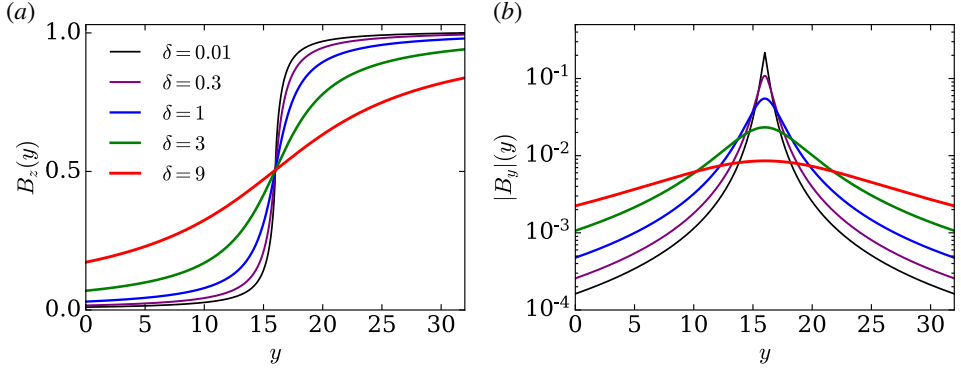


FIGURE 2. Distribution of mean profiles of (a) vertical magnetic field  $B_z(y)$  and (b) absolute value of the horizontal magnetic field  $|B_y|(y)$  along the lengthwise direction for different  $\delta$ . The magnetic field profiles are normalized by the maximum value of their vertical component, which is at  $y \rightarrow \infty$ .

and electrical potential respectively, and  $\tilde{\mathbf{B}}$  is the applied magnetic field normalized by  $B_{z,max}$ , which is the maximum value of the vertical component of the magnetic field (at  $y \rightarrow \infty$ ). The governing equations are made dimensionless by using the cell height  $H$ , the imposed temperature difference  $\Delta$ , and the free-fall velocity  $U = \sqrt{\alpha g \Delta H}$  (where  $g$  and  $\alpha$  are respectively the gravitational acceleration and the volumetric coefficient of thermal expansion of the fluid). The nondimensional governing parameters are the Rayleigh number ( $Ra$ ), the Prandtl number ( $Pr$ ), and the Hartmann number ( $Ha_{z,max}$ ) based on  $B_{z,max}$ . These parameters are defined as follows:

$$Ra = \frac{\alpha g \Delta H^3}{\nu \kappa}, \quad Pr = \frac{\nu}{\kappa}, \quad Ha_{z,max} = B_{z,max} H \sqrt{\frac{\sigma}{\rho \nu}}, \quad (2.9)$$

where  $\nu$  is the kinematic viscosity,  $\kappa$  is the thermal diffusivity,  $\rho$  is the density, and  $\sigma$  is the electrical conductivity of the fluid. In the next section, we describe the simulation details.

## 2.2. Numerical method

We conduct direct numerical simulations of thermal convection in a rectangular cell of dimensions  $l_x \times l_y \times H = 16 \times 32 \times 1$  under the influence of a magnetic field which is a function of space. The spatial distribution of the magnetic field is given by equations (2.1) to (2.3). We use a second-order finite difference code developed by Krasnov *et al.* (2011) to numerically solve equations (2.4) to (2.8) on a grid-resolution of  $4800 \times 9600 \times 300$  points. The Rayleigh, Prandtl, and maximum Hartmann numbers are fixed to  $Ra = 10^5$ ,  $Pr = 0.021$ , and  $Ha_{z,max} = 120$ , respectively. The mesh is non-uniform in the  $z$ -direction with stronger clustering of the grid points near the top and bottom boundaries. The elliptic equations for pressure, electric potential, and the temperature are solved based on applying cosine transforms in  $x$  and  $y$  directions and using a tridiagonal solver in the  $z$  direction. The diffusive term in the temperature transport equation is treated implicitly. The time discretization of the momentum equation uses the fully explicit Adams-Bashforth/Backward-Differentiation method of second order (Peyret 2002). A constant time step size of  $1 \times 10^{-4}$  free fall time units was chosen for our simulations, which satisfied the Courant-Friedrichs-Lowy (CFL) condition for all runs.

All the walls are rigid and electrically insulated such that the electric current density  $\mathbf{j}$  forms closed field lines inside the cell. The top and bottom walls are held fixed at

---

Runs	$\delta$	$Re_{global}$	$Nu_{global}$	$t_N$
1	0.01	$763 \pm 2$	$1.80 \pm 0.01$	20
2	0.3	$767 \pm 5$	$1.82 \pm 0.01$	20
3	1	$715 \pm 4$	$1.75 \pm 0.01$	21
4	3	$644 \pm 3$	$1.72 \pm 0.01$	20
5	9	$474 \pm 3$	$1.60 \pm 0.01$	20

TABLE 1. Parameters of the simulations: the gap ( $\delta$ ) between the magnetic poles and the conducting walls, the global Reynolds number ( $Re_{global}$ ), the global Nusselt number ( $Nu_{global}$ ), and the number of free-fall time units ( $t_N$ ) run by the solver after attaining statistically steady state.  $Re_{global}$  and  $Nu_{global}$  are averaged over  $t_N$  timeframes and the errors are the standard deviations of the above quantities. The Rayleigh number, Prandtl number, and the maximum Hartmann number are fixed to  $Ra = 10^5$ ,  $Pr = 0.021$ , and  $Ha_{z,max} = 120$  respectively.

---

$T = -0.5$  and  $T = 0.5$  respectively, and the sidewalls are adiabatic with  $\partial T / \partial \eta = 0$  (where  $\eta$  is the component normal to sidewall).

Table 1 lists the important parameters of our simulation runs. In this table, we also report the turbulent momentum transfer quantified by the global Reynolds number ( $Re_{global}$ ) and the turbulent heat transport quantified by the global Nusselt number ( $Nu_{global}$ ). These quantities are given by

$$Re_{global} = u_{rms} \sqrt{Ra/Pr}, \quad (2.10)$$

$$Nu_{global} = 1 + \sqrt{RaPr} \langle u_z T \rangle_{V,t_N}, \quad (2.11)$$

where  $\langle \cdot \rangle$  represents averaging,  $u_{rms} = \sqrt{\langle u_x^2 + u_y^2 + u_z^2 \rangle_{V,t_N}}$  with  $V$  being the volume of the convection cell, and  $t_N$  (also reported in table 1) is the number of free-fall times run by the solver after attaining a statistically steady state.

In turbulent magnetohydrodynamics with vertical magnetic fields, four boundary layers are formed: 1) viscous boundary layers near all the walls, 2) thermal boundary and 3) Hartmann layers near the top and bottom walls, and 4) Shercliff layers near the sidewalls. Figure 3 exhibits a sketch of the different types of boundary layers. In order to obtain accurate results, it is important that all these layers are adequately resolved. In our cases, although the imposed magnetic field has a horizontal component as well, it is very small compared to the vertical component near the sidewalls. Hence, the sidewalls have been considered to contain only the Shercliff layers and no Hartmann layers. It must also be noted that the thicknesses of all the boundary layers vary along the  $y$  direction because they depend on the local Hartmann number, which, in turn, affects the Reynolds and Nusselt numbers. Thus, for a conservative resolution analysis, the minimum thickness of these boundary layers has been considered. These are given by

$$\delta_{T,min} = \frac{1}{2Nu_{max}}, \quad (2.12)$$

$$\delta_{u,min} = \frac{1}{4\sqrt{Re_{max}}}, \quad (2.13)$$

$$\delta_{H,min} = \frac{1}{Ha_{z,max}}, \quad (2.14)$$

$$\delta_{S,min} = \frac{1}{\sqrt{Ha_{z,max}}}, \quad (2.15)$$

where  $\delta_{T,min}$ ,  $\delta_{u,min}$ ,  $\delta_{H,min}$ , and  $\delta_{S,min}$  are the minimum thicknesses of thermal bound-

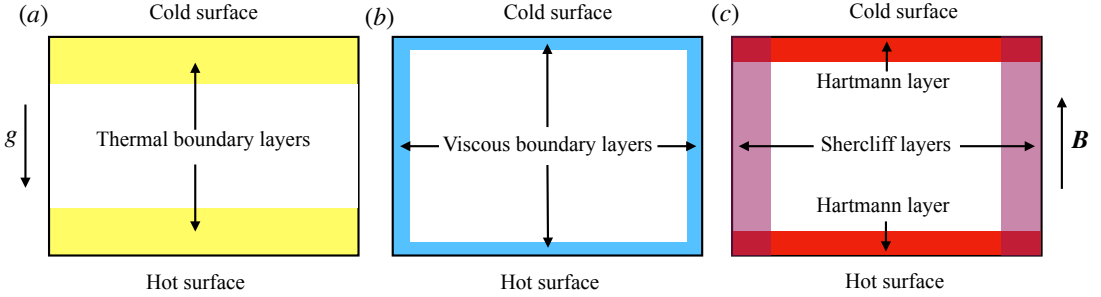


FIGURE 3. Sketches of the vertical cross section of a Rayleigh-Bénard convection cell under vertical magnetic field showing (a) thermal boundary layers, (b) viscous boundary layers, and (c) Hartmann and Shercliff layers.

ary layers, viscous boundary layers, Hartmann layers, and the Shercliff layers, respectively. Here, we also remark that although the relation for the viscous boundary layer thickness given by  $\delta_u \sim Re^{-1/2}$  is not very accurate (see, for example, Breuer *et al.* 2004; Scheel *et al.* 2012; Bhattacharya *et al.* 2021), it provides a reasonable estimate for small Prandtl number convection. Further,  $Nu_{max}$  and  $Re_{max}$  respectively denote the Nusselt and Reynolds numbers integrated over the regions where  $B_z(x, y, z) < 0.1B_{z,max}$  and are computed to be  $Nu_{max} = 2.66$  and  $Re_{max} = 1115$ . Based on the above values, we have a minimum of 12 points, 76 points, and 12 points, respectively, in the viscous boundary layers, thermal boundary layers, and in the Hartmann layers adjacent to the top and bottom walls; and 28 points in the Shercliff layer adjacent to the sidewalls. Thus, our simulations are well resolved and also satisfy the resolution criterion of Grötzsch (1983) and Verzicco & Camussi (2003). In the next section, we discuss our results in detail.

### 3. Results

In this section, we discuss the characteristics of the large-scale convection patterns, the spatial profile of the large-scale momentum and the global heat transport, and the wall-attached convection in the regions of strong magnetic flux. For our analysis, we introduce the local vertical Hartmann number  $Ha_z(y)$  which is defined as,

$$Ha_z(y) = Ha_{z,max} \frac{\langle B_z \rangle_{x,z}}{B_{z,max}}, \quad (3.1)$$

where  $B_z$  is the vertical component of the local magnetic field. Thus,  $Ha_z(y)$  quantifies the strength of  $B_z$  averaged over the corresponding  $x$ - $z$ -plane. We will discuss the variations of the heat and momentum transport with  $Ha_z(y)$  and their resulting impact on the global dynamics.

#### 3.1. Large-scale structures

We use our numerical data to analyse the flow structures in the convection cell for different fringe-widths. Figures 4(a)-(e) exhibit the density plots of temperature field on the horizontal midplane for  $\delta = 0.01$  to 9. The corresponding density plots of the vertical velocity field are shown in figures 4(f)-(g). The data for the above plots are averaged over 20 to 21 timeframes (see table 1). The figures show that bulk convection is completely suppressed in the regions of strong magnetic fields. The region of suppressed bulk convection becomes smaller as  $\delta$  is increased. This is expected because for large

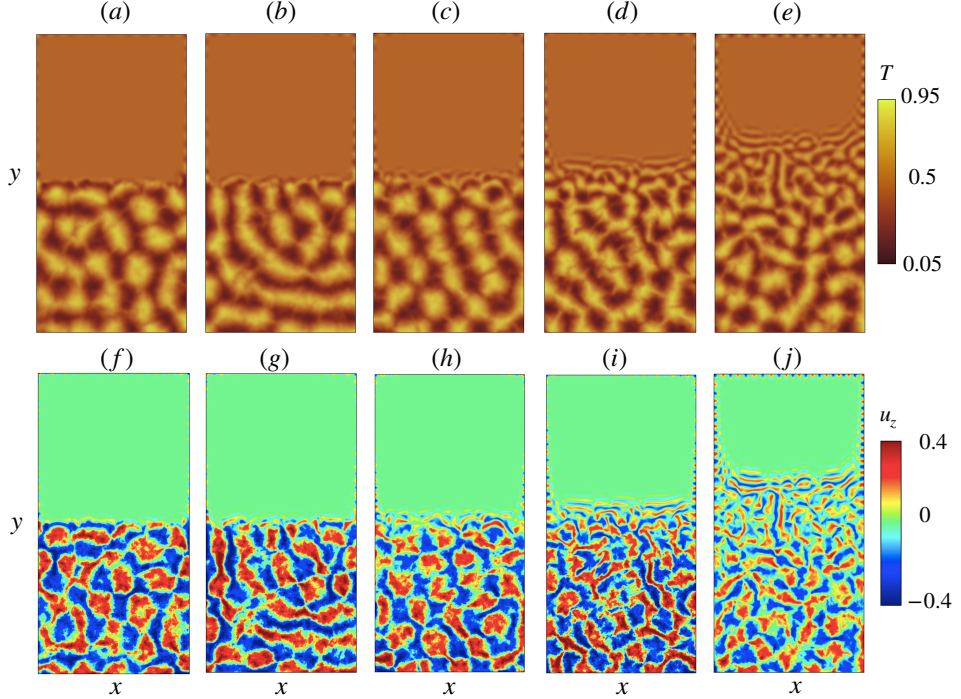


FIGURE 4. Density plots of time-averaged fields on the horizontal midplane for different fringe-widths of the imposed magnetic field. Plots of the temperature field for (a)  $\delta = 0.01$ , (b)  $\delta = 0.3$ , (c)  $\delta = 1$ , (d)  $\delta = 3$ , and (e)  $\delta = 9$ . Plots of the vertical velocity field for (f)  $\delta = 0.01$ , (g)  $\delta = 0.3$ , (h)  $\delta = 1$ , (i)  $\delta = 3$ , and (j)  $\delta = 9$ . The flows are organized into large-scale patterns that extend over scales larger than the domain height.

$\delta$ , the gradient of the magnetic field is small and hence the region with  $Ha_z(y)$  above the critical Hartmann number ( $Ha_{z,c}$ ) is also small. Note that for our runs, that is, for  $Ra = 10^5$ , the critical Hartmann number computed using the linear stability analysis of Chandrasekhar (1981) is  $Ha_{z,c} = 88.7$ .

Figures 4(a–j) also show that in the regions of  $Ha_z(y) < Ha_{z,max}$ , the flow gets organized into superstructures. The superstructures observed in the above figures in the weak magnetic flux regions are qualitatively similar to those observed by Pandey *et al.* (2018) for  $Pr = 0.021$ . Further, the superstructures are relatively isotropic in the regions of weak magnetic flux, that is, they do not show any preference towards specific orientations. However, as the strength of the vertical magnetic field increases, the superstructures become more elongated and align themselves perpendicular to the sidewalls. The change in spatial structure of the flow is more clearly visible for  $\delta = 9$ , in which the vertical magnetic field changes gradually. The transition in the orientation of the superstructures begins to occur for  $Ha_z(y) \approx 0.8Ha_{z,c}$  where the flow is dominated by ascending and descending planar jets originating from the sidewalls. The flow structures in this regime are very similar to those observed by Akhmedagaev *et al.* (2020b) in their simulation data of RBC in a cylindrical cell under strong uniform vertical magnetic field. They can be attributed to quasi-two-dimensional vortex sheets which are often found in magnetohydrodynamic flows with strong magnetic fields (Zikanov & Thess 1998). As one moves further towards stronger magnetic flux region, the structures originating from the

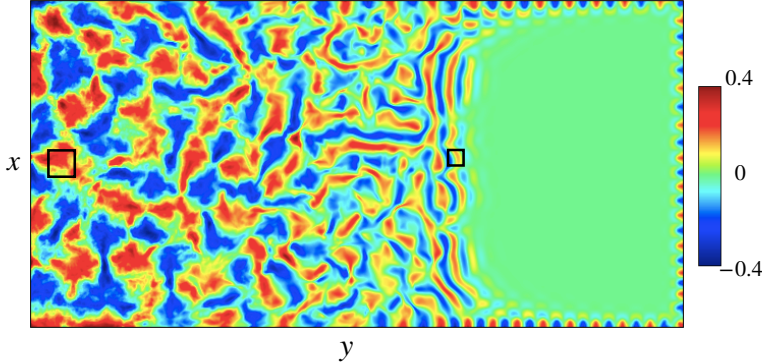


FIGURE 5. Density plot of time-averaged vertical velocity field on the horizontal midplane for  $\delta = 9$ . The length scale of the convection patterns becomes smaller along the direction of increasing magnetic field and can be indicated by the minimum length scale  $\lambda(y)$  computed based on the stability analysis of Chandrasekhar (1981). The two squares of side  $\lambda(y)$  represent the minimum length scale in the points of their respective locations in the domain.

sidewalls extend less into the bulk, until for  $Ha_z(y) \gtrsim Ha_{z,c}$ , the flow is confined only near the sidewalls. These wall-attached flows will be discussed in detail in § 3.3.

It can be visually observed that the length scale of the convection patterns decreases along the direction of increasing magnetic field. The theoretical lower limit of the length scale at different regions of the convection domain can be computed using the linear stability analysis of Chandrasekhar (1981). This limiting scale, represented by  $\lambda$ , is a function of the local Hartmann number and corresponds to the dimension of the rolls at the onset of convection at that Hartmann number. We estimate  $\lambda$  at two points on the horizontal midplane. The first point is at  $y = 2$  where the magnetic field is weak with  $Ha_z(y) \approx 0.25 Ha_{z,c}$ . The second point is at  $y = 22$  where  $Ha_z(y) \approx Ha_{z,c}$ . The density plot of  $u_z$  is redrawn in figure 5 and  $\lambda$  is represented at the above two points by black squares of side length  $\lambda$ . The square in the weak magnetic flux region (with  $\lambda = 1.23$ ) is visibly larger than the one in the strong magnetic flux region ( $\lambda = 0.76$ ), with the size of the patterns being roughly the same as the size of the squares. Thus, the length scales of the patterns are close to the theoretical limits based on linear stability analysis.

We now quantitatively analyse the isotropy of the flow using our numerical data. Towards this objective, we compute the following quantities: the local vertical anisotropy parameter  $2E_z(y)/E_h(y)$ , the local horizontal anisotropy parameter  $E_y(y)/E_x(y)$ , and the ratio of the kinetic energies along the  $z$  and  $y$  directions. In the above,  $E_z(y) = 0.5\langle u_z^2 \rangle_{x,z}$  is the vertical kinetic energy,  $E_h(y) = 0.5\langle u_x^2 + u_y^2 \rangle_{x,z}$  is the horizontal kinetic energy,  $E_x(y) = 0.5\langle u_x^2 \rangle_{x,z}$  is the kinetic energy along  $x$  direction, and  $E_y(y) = 0.5\langle u_y^2 \rangle_{x,z}$  is the kinetic energy along the  $y$  direction, all averaged over the  $x-z$  plane. To understand the variation of flow anisotropy with magnetic field strength, the planar kinetic energy,  $E(y) = 0.5\langle u_x^2 + u_y^2 + u_z^2 \rangle_{x,z}$ , along with the aforementioned anisotropy factors, are plotted versus  $Ha_z(y)$ . The plots are exhibited in figures 6(a-d). Figure 6(a) shows that the local kinetic energy decreases with  $Ha_z(y)$ , as expected.

The flow is roughly isotropic in the regions of weak vertical magnetic field corresponding to  $Ha_z(y) < 0.3 Ha_{z,c}$ , as evident from figures 6(b-d). However, as shown in figures 6(b) and (d), the vertical velocity fluctuations become more dominant compared to the horizontal ones with increasing  $Ha_z(y)$ . This property is consistent with the

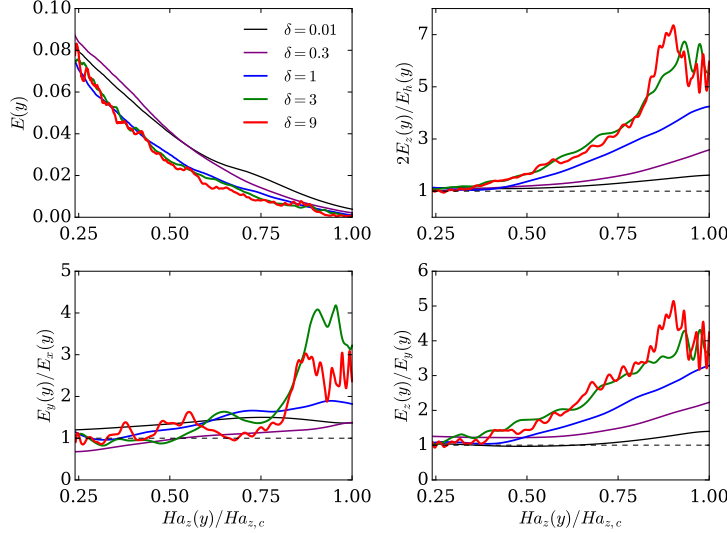


FIGURE 6. Mean profiles of (a) the local kinetic energy  $E(y)$ , (b) the local vertical anisotropy parameter  $2E_z(y)/E_h(y)$ , (c) the local horizontal anisotropy parameter  $E_y(y)/E_x(y)$ , and (d) the ratio of the kinetic energy along  $z$  and  $y$  directions versus the Hartmann number,  $Ha_z(y)$ , based on the mean vertical magnetic field  $B_z(y)$ . Both, the vertical and the horizontal anisotropy parameters increase with the local vertical magnetic field strength.

anisotropy observed by Yan *et al.* (2019) and Akhmedagaev *et al.* (2020b) for strong Hartmann number convection with uniform magnetic fields, and is reminiscent of the stable cellular regime described by Zürner *et al.* (2020). The anisotropy becomes more pronounced as the fringe-width, governed by  $\delta$ , increases. This might be due to the fact that when the fringe zone is large, the velocity structures get more space to change their orientations.

For strong magnetic fields, there is anisotropy among the horizontal components of velocity as well. Figure 6(c) shows that for  $Ha_z(y) > 0.65Ha_{z,c}$ ,  $E_y(y)$  begins to dominate  $E_x(y)$ , implying that the velocity fluctuations in the  $y$  direction are stronger compared to that in the  $x$  direction. This is also consistent with figures 4(a–j) which show that for moderately strong Hartmann numbers, the superstructure rolls orient themselves perpendicular to the longitudinal sidewalls. In the next subsection, we discuss the effects of the fringing magnetic fields on the local as well as global momentum and heat transport.

### 3.2. Heat and momentum transport

We analyze the spatial variation of the large-scale heat and momentum transport in our numerical setup. Towards this objective, we first compute the local planar Reynolds number  $Re(y)$  and Nusselt number  $Nu(y)$  for every  $\delta$ . These are given by

$$Re(y) = \sqrt{\frac{Ra}{Pr}} \langle u_x^2 + u_y^2 + u_z^2 \rangle_{x,z,t_N}^{1/2}, \quad Nu(y) = 1 + \sqrt{RaPr} \langle u_z T \rangle_{x,z,t_N}. \quad (3.2)$$

It must be noted that in order to avoid clutter,  $Nu(y)$  and  $Re(y)$  are computed for every 120th  $x$ - $z$ -plane. Moreover,  $Nu(y)$  exhibits strong spatial fluctuations even after averaging over all the timeframes; these fluctuations are smoothed by computing the moving average of  $Nu(y)$  using a window-size of 5  $x$ - $z$ -planes.

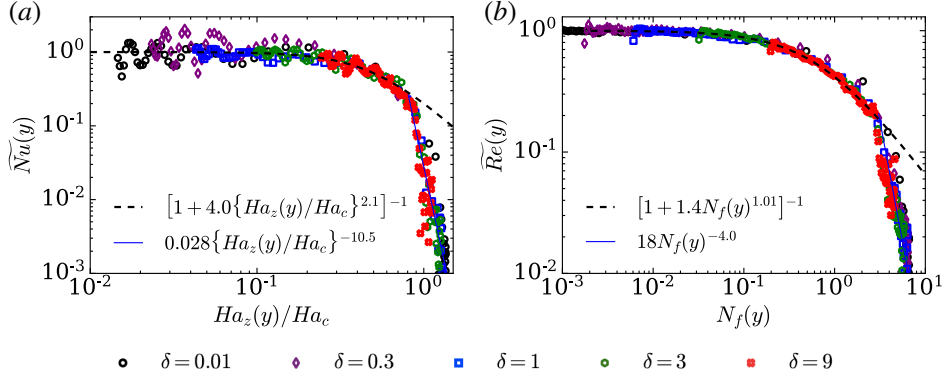


FIGURE 7. Variations of the Nusselt and Reynolds numbers with the local vertical magnetic field strengths. For  $\delta = 0.01$  to 9: (a) normalized local Nusselt number,  $\widetilde{Nu}(y)$ , versus the normalized local Hartmann number,  $Ha_z(y)/Ha_{z,c}$ , based on vertical magnetic field strength; and (b) normalized local Reynolds number,  $\widetilde{Re}(y)$ , versus the local free-fall interaction parameter,  $N_f(y)$ . The best-fit curves for the above data are also shown.

Taking inspiration from the recent experimental work of Zürner *et al.* (2020) on thermal convection under uniform vertical magnetic fields, we plot the normalized local Nusselt number  $\widetilde{Nu}(y)$  versus the normalized local vertical Hartmann number  $Ha_z(y)/Ha_{z,c}$ . The normalized local Nusselt number is given by

$$\widetilde{Nu}(y) = \frac{Nu(y) - 1}{Nu_{max} - 1}, \quad (3.3)$$

where  $Nu_{max} = 2.66$  (see § 2.2). Figure 7(a) shows that for all  $\delta$ , the points collapse well into a single curve, thus showing a universal dependence of  $Nu(y)$  on  $Ha_z(y)$ . The plot shows that for  $Ha_z(y) \lesssim 0.3Ha_{z,c}$ , the Nusselt number does not change significantly and remains close to its maximum value. This regime corresponds to the turbulent and isotropic regime. For  $Ha_z(y) \gtrsim 0.3Ha_{z,c}$ , the flow transitions into the cellular regime (as per the nomenclature of Zürner *et al.* 2020) and the local Nusselt number starts to drop sharply as  $Ha_z(y)$  increases. For  $Ha_z(y) < 0.85Ha_{z,c}$ , the best fit curve for our data is

$$\widetilde{Nu}(y) = \left[ 1 + \chi_1 \left\{ \frac{Ha_z(y)}{Ha_{z,c}} \right\}^{\gamma_1} \right]^{-1}, \quad (3.4)$$

where  $\chi_1 = 4.0 \pm 0.7$  and  $\gamma_1 = 2.1 \pm 0.3$ . The values of  $\chi_1$  and  $\gamma_1$  are interestingly very close to those observed by Zürner *et al.* (2020) for uniform magnetic fields. For  $Ha_z(y) > 0.85Ha_{z,c}$ ,  $\widetilde{Nu}(y)$  decreases more steeply than (3.4) and is described by the following power law,

$$\widetilde{Nu}(y) = 0.028 \left\{ \frac{Ha_z(y)}{Ha_{z,c}} \right\}^{-10.5 \pm 0.9}. \quad (3.5)$$

This regime corresponds to the wall-mode regime in which the flow gets further suppressed and begins to confine itself near the sidewalls. It must be noted that the Zürner *et al.* (2020) could not obtain a best-fit expression for  $Nu$  in the wall-mode regime due to lack of data close to the wall.

We conduct a similar analysis for  $Re(y)$  as well. We compute the normalized Reynolds

number given by

$$\widetilde{Re}(y) = \frac{Re(y)}{Re_{max}}, \quad (3.6)$$

where  $Re_{max} = 1115$  (see § 2.2). The results of Zürner *et al.* (2020) suggest that  $\widetilde{Re}(y)$  should scale as  $Ha_z(y)/\sqrt{Ha_{z,c}}$  instead of  $Ha_z(y)/Ha_{z,c}$ . Therefore, for our analysis, we use the local free-fall interaction parameter  $N_f(y)$ , which is given by

$$N_f(y) = \frac{Ha_z(y)^2}{Re_f}, \quad (3.7)$$

where  $Re_f = \sqrt{Ra/Pr}$  is the free-fall Reynolds number. Using the approximate relation of  $Ha_{z,c} \approx \sqrt{Ra}/\pi$ , we get

$$N_f(y) = Ha_z(y)^2 \frac{\pi}{\sqrt{Ra}} \frac{\sqrt{Pr}}{\pi} \approx \frac{Ha_z(y)^2}{Ha_{z,c}} \frac{\sqrt{Pr}}{\pi} \sim \frac{Ha_z(y)^2}{Ha_{z,c}}. \quad (3.8)$$

The above relation shows that  $N_f(y)$  is proportional to  $Ha_z(y)^2/Ha_{z,c}$ , implying that  $\widetilde{Re}(y)$  scales with  $N_f(y)$ . Thus, we plot  $\widetilde{Re}(y)$  versus  $N_f(y)$ . The plot in figure 7(b) shows that, similar to the Nusselt number, the data points for all  $\delta$  collapse into a single curve. For  $N_f(y) < 0.17$ , which corresponds to  $Ha_z(y) < 0.22Ha_{z,c}$ , the Reynolds number retains its maximum value ( $Re_{max}$ ). At higher  $N_f(y)$ , the Reynolds number starts to fall sharply with the interaction parameter. For  $N_f(y) < 3.2$ , which corresponds to  $Ha_z(y) < 0.95Ha_{z,c}$ , the best fit curve for our data is given by

$$\widetilde{Re}(y) = [1 + \chi_2 \{N_f(y)\}^{\gamma_2}]^{-1}, \quad (3.9)$$

with  $\chi_2 = 1.40 \pm 0.03$  and  $\gamma_2 = 1.01 \pm 0.03$ . The value of  $\gamma_2$  is again very close to that observed by Zürner *et al.* (2020) for uniform magnetic fields. For  $Ha_z(y) > 0.95Ha_{z,c}$ , which corresponds to the wall-attached convection regime,  $\widetilde{Re}(y)$  falls even more steeply than (3.9) and is described by the following power law,

$$\widetilde{Re}(y) = 18N_f(y)^{-4.0 \pm 0.2}. \quad (3.10)$$

Having studied the local variations of heat and momentum transport, we now analyze the global Reynolds and Nusselt numbers ( $Re_{global}$  and  $Nu_{global}$  respectively) and their dependence on  $\delta$ . These global quantities are computed numerically using equations (2.10) and (2.11) from our simulation data and are plotted versus  $\delta$  in figures 8(a) and (b) as black squares. The figures show that both  $Re_{global}$  and  $Nu_{global}$  decrease as  $\delta$  increases. This result is counter intuitive because for large  $\delta$ , bulk convection is completely ceased only in a small region (as seen in figure 4) and hence one would expect the overall heat and momentum transport to be stronger. However, a careful look at figure 2(a) reveals that the vertical magnetic field is stronger in the weak magnetic flux region for large fringe-widths, which, in turn, weakens convection in that region. The increase in convection in the strong magnetic flux region is unable to compensate the suppression of convection in the weak magnetic flux region, resulting in a decrease of overall heat and mass transport for large fringe-widths.

The above results, however, do not indicate whether such a variation of global Reynolds and Nusselt numbers with  $\delta$  holds for all  $Ha_{z,max}$ . To explore this aspect, we need to estimate  $Re_{global}$  and  $Nu_{global}$  for a given value of  $Ha_{z,max}$  and  $\delta$ . Towards this objective, we make use of the best fit relations for  $Nu(y)$  and  $Re(y)$  given by equations (3.4), (3.5), (3.9), and (3.10) obtained earlier, and numerically integrate them over the entire domain

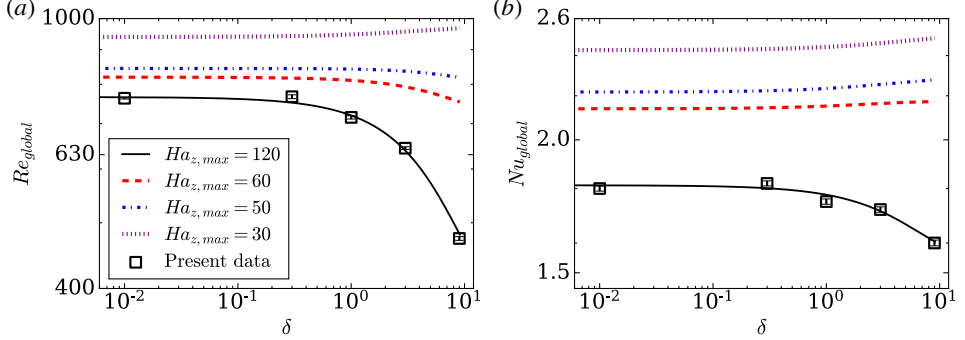


FIGURE 8. Plots of (a) the global Reynolds number  $Re_{global}$  (black squares), computed from our numerical data using equation (2.10), versus  $\delta$ , and (b) the global Nusselt number  $Nu_{global}$  (black squares), computed from our numerical data using equation (2.11), versus  $\delta$ . Also shown in the plots are the estimates (solid curves) of  $Re_{global}$  and  $Nu_{global}$  computed using equations (3.11) and (3.12) for different values of  $Ha_{z,max}$ .

to estimate global Reynolds and Nusselt numbers as follows:

$$Re_{global} = \frac{1}{l_y} \int_0^{l_y} Re(y) dy = \frac{1}{l_y} \int_0^{l_y} Re(Ha_z(y)) dy, \quad (3.11)$$

$$Nu_{global} = \frac{1}{l_y} \int_0^{l_y} Nu(y) dy = \frac{1}{l_y} \int_0^{l_y} Nu(Ha_z(y)) dy, \quad (3.12)$$

where it can be recalled that

$$Ha_z(y) = Ha_{z,max} \frac{\langle B_z \rangle_{x,z}}{B_{z,max}},$$

and  $B_z = B_z(x, y, z, \delta)$  is given by equation (2.3). Thus, for given  $Ha_{z,max}$  and  $\delta$ , one can estimate  $Re_{global}$  and  $Nu_{global}$  using equations (3.11) and (3.12). We compute these estimates for  $Ha_{z,max} = 120, 60, 50$ , and  $30$ , and for  $\delta$  ranging from  $0.005$  to  $9.1$  in increments of  $0.01$ . The estimated values of  $Re_{global}$  and  $Nu_{global}$  are plotted versus  $\delta$  in figures 8(a) and (b) as solid curves. The curves for  $Ha_{z,max} = 120$  fit the data points of directly computed  $Re_{global}$  and  $Nu_{global}$  (black squares) very well, implying that equations (3.11) and (3.12) provide fairly accurate estimates.

Figure 8(a) also shows that the decrease of  $Re_{global}$  with  $\delta$  becomes less apparent with a decrease of  $Ha_{z,max}$ . In fact, for  $Ha_{z,max} = 30$ ,  $Re_{global}$  increases marginally with  $\delta$ . Figure 8(b) indicates that  $Nu_{global}$  increases with  $\delta$  for  $Ha_{z,max} = 60, 50$ , and  $30$ , with the above increase becoming more apparent with the decrease of  $Ha_{z,max}$ . It is therefore clear that for smaller maximum magnetic field strengths, the overall heat and momentum transport increases with the increase of fringe-width. This implies that for small values of  $Ha_{z,max}$ , the suppression of convection in the weak magnetic flux region is small compared to the increase of convection in the strong magnetic flux region. Thus, we can conclude that the variation of  $Re_{global}$  and  $Nu_{global}$  with the fringe-width depends critically on  $Ha_{z,max}$ . Finally, we discuss the dynamics of wall-attached convection in the strong magnetic flux region in the next subsection.

### 3.3. Wall-attached convection

We plot the time-averaged isosurfaces of  $u_z = 0.01$  (red) and  $u_z = -0.01$  (blue) for  $\delta = 1$  and  $\delta = 9$  in figures 9(a) and (b) respectively. The figures show that in

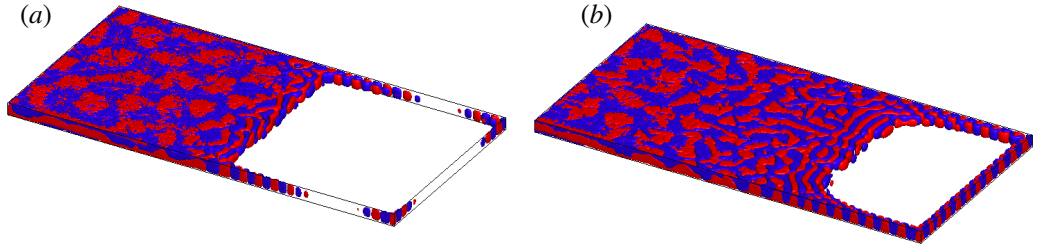


FIGURE 9. Isosurfaces of  $u_z = 0.01$  (red) and  $u_z = -0.01$  (blue) for (a)  $\delta = 1$  and (b)  $\delta = 9$ . In the regions with strong magnetic fields, convective motions are confined near the sidewalls.

the strong magnetic flux region, the flow in the bulk is completely suppressed with alternating up-and downwelling flow regions attached to the sidewalls. The structure of the wall-modes is consistent with that observed by Liu *et al.* (2018) in their simulations of thermal convection in a rectangular domain with uniform vertical magnetic field. However, unlike for rotating convection (Horn & Schmid 2017; Zhang *et al.* 2020) or convection in cylindrical domains (Akhmedagaev *et al.* 2020b), the wall modes do not oscillate or move along the sidewalls (Grannan *et al.* 2022; Schumacher 2022).

The wall-modes are dense and uniformly distributed along the sidewalls for  $\delta = 9$ . However, for  $\delta = 1$ , the wall modes are visibly thinner with the isosurfaces clustering more towards the corners instead of being uniformly distributed along the sidewalls. The clustering occurs because of weaker Lorentz force in the corners, which, in turn, results due to the electric current getting further constrained by the two insulated sidewalls in proximity of each other. The above trend in the local differences of the wall modes is also observed for  $\delta = 0.01, 0.3$ , and  $3$  as shown later in this section.

For each sidewall in the strong magnetic flux region, we compute the mean distance  $\bar{\delta}_w$  of the wall modes from the sidewall. This distance is computed as follows,

$$\bar{\delta}_w = \frac{\int \delta_w u_{z,max} dl}{\int u_{z,max} dl}, \quad (3.13)$$

where  $dl = dy$  for the longitudinal sidewall and  $dl = dx$  for the lateral sidewall. In the above,  $\delta_w$  is the shortest distance between the sidewall and the point of maximum absolute velocity  $u_{z,max}$  adjacent to the sidewall, and the summations are over the regions where  $Ha_z(y) > Ha_{z,c}$ . Thus,  $\bar{\delta}_w$  is the weighted average of the shortest distance between the point of maximum absolute velocity and the sidewall, with the maximum absolute velocity being the weights. We also compute the mean distance averaged over all the sidewalls. We plot the mean distances for each sidewall as well as the overall mean distance versus  $\delta$  in figure 10. The figure shows that the wall modes are in general more attached to the lateral sidewall ( $y = 32$ ) compared to the longitudinal sidewalls ( $x = 0$  and  $x = 16$ ). There is, however, no clear trend regarding the variation of  $\bar{\delta}_w$  with the fringe-width.

We further analyze the amplitudes of the wall modes along the three sidewalls for our runs. Towards this objective, we measure the vertical velocity field at every point on the horizontal midplane at a distance of  $\bar{\delta}_w$  from the sidewalls. We plot this vertical velocity profile along every sidewall in figure 11. The figure shows that with the exception of  $\delta = 9$ , the amplitudes of the wall modes are stronger near the corners and become weaker as one moves away from the corners. This behavior in the amplitudes is consistent with figure 9(a) which shows that the wall-modes are clustered in the corners. As explained earlier, these local differences in amplitudes occur due the current being more constrained

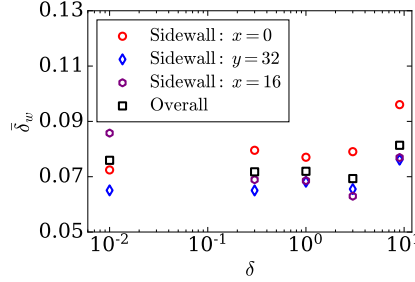


FIGURE 10. The average distance between the wall modes and the sidewalls versus  $\delta$  in the regions of  $Ha_z(y) > Ha_{z,c}$ . The wall modes are more attached to the lateral sidewalls than the longitudinal sidewalls.

in the corners resulting in weaker convection-suppressing Lorentz force in these regions. Figure 11 also shows that near the corners, the amplitudes of the wall modes grow with an increase of  $\delta$ . However, in the regions away from the corners, the amplitudes decrease as  $\delta$  is decreased from 9 to 1; and then increases with a further decrease of  $\delta$ . For  $\delta = 0.3$  and 1, the amplitudes become negligible small away from the corners. However, for  $\delta = 0.01$ , although the amplitudes of the modes away from the corners are smaller than those near the corners, they are larger than the amplitudes of wall modes away from the corners for  $\delta = 0.3$  and 1.

The reason for the non-monotonic behavior of wall-modes with  $\delta$  away from the corners is not yet clear. A possible explanation is that in addition to the vertical component of the magnetic field  $B_z$ , the horizontal component  $B_y$  also plays a role in stabilizing convection near the sidewalls. From figure 2(b), it can be seen that for small  $\delta$  or fringe-width, although  $B_y$  is strong in  $y = l_y/2$  midplane, it falls sharply and becomes very small as one moves away from the midplane. Thus, for  $\delta = 0.01$ ,  $B_y$  is too weak to stabilize convection near the sidewalls at  $y \gg l_y/2$ , resulting in sustained wall-attached convection. On the other hand, for large  $\delta$ ,  $B_y$  in the regions away from  $y = l_y/2$  midplane is not as weak as that for small  $\delta$ . Thus, as  $\delta$  is increased up to  $\delta = 1$ ,  $B_y$  becomes stronger and suppresses wall-attached convection. On further increasing  $\delta$ , although  $B_y$  grows only marginally,  $B_z$  becomes too weak to suppress wall-attached convection. Hence, we get prominent wall modes again for  $\delta = 3$  and 9. The non-monotonic behavior of wall-modes will be explored in detail in a future study.

#### 4. Summary and conclusions

In this paper, we performed detailed numerical simulations of turbulent convection of a horizontally extended domain under the influence of fringing magnetic fields. The magnetic field is generated in the gap between semi-infinite poles of permanent magnets, with the convection domain located near the edge of the gap. The quasi-static approximation of magnetohydrodynamics is applied. We kept the Rayleigh number, Prandtl number, and the maximum Hartmann number fixed at  $Ra = 10^5$ ,  $Pr = 0.021$ , and  $Ha_{z,max} = 120$  respectively, and varied the fringe-width by controlling the gap  $\delta$  between the magnetic poles and the thermal plates. We analysed the spatial distribution of large-scale convection patterns, heat and momentum transport, and wall-attached convection, and their variations with the magnetic field profiles.

The convection patterns are found to comprise of structures whose horizontal dimen-

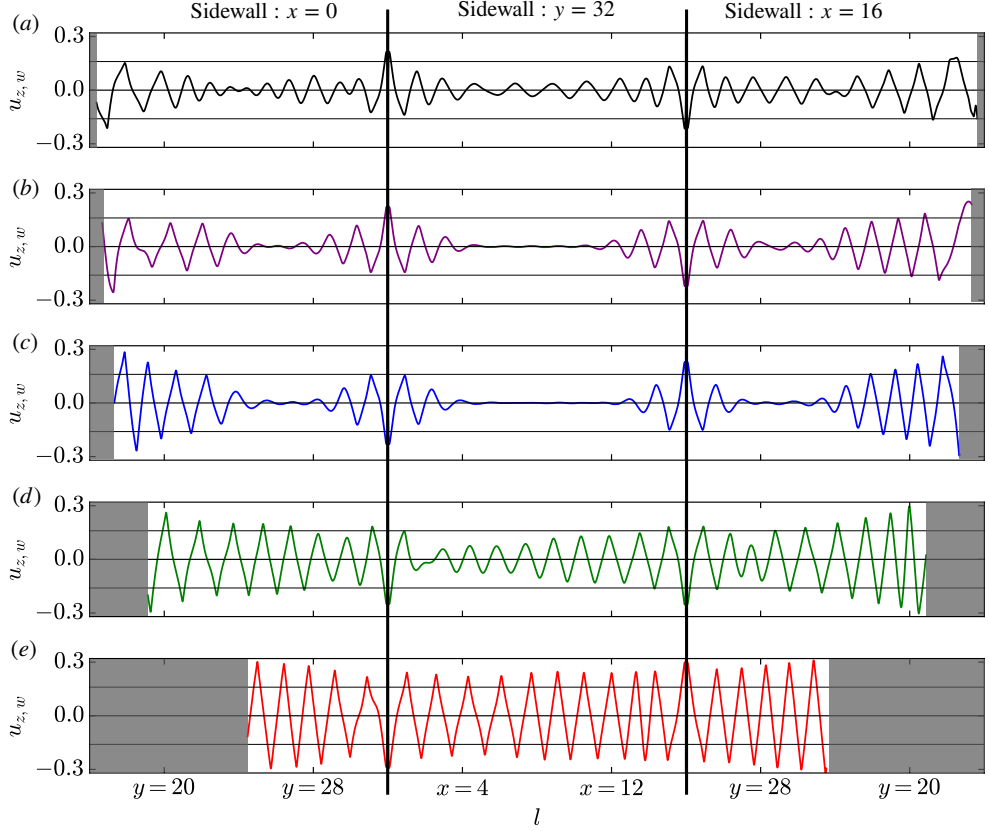


FIGURE 11. Vertical velocity  $u_{z,w}$  measured on the horizontal midplane at distance of  $\bar{\delta}_w$  from the sidewalls in the regions of  $Ha(y) > Ha_c$  (nonshaded regions) for (a)  $\delta = 0.01$  (black curve), (b)  $\delta = 0.3$  (purple curve), (c)  $\delta = 1$  (blue curve), (d)  $\delta = 3$  (green curve), and (e)  $\delta = 9$  (red curve). The shaded regions correspond to  $Ha_z(y) < Ha_{z,c}$  where the flow is not fully suppressed in the bulk. The amplitudes of the wall modes in the regions away from the corners exhibit a non-monotonic dependence on  $\delta$ . Note that the above plots are resolved by a total of at least 9000 grid points in the horizontal direction.

sions are larger than the domain height. These structures do not exhibit any preferred orientation in regions of weak magnetic field, but become aligned perpendicular to the longitudinal sidewalls in the fringe zone. Further, the flow progressively becomes anisotropic towards the vertical direction in the fringe zone.

We obtained the best-fit relations for local Reynolds and Nusselt number as a function of the local Hartmann number that are valid for any fringe-width. We integrated these relations over the entire domain to estimate the global Reynolds and Nusselt numbers for different values of  $Ha_{z,max}$ . The variation of the above global quantities with fringe-width was shown to depend on  $Ha_{z,max}$  and is governed by the balance between the convective motion in the weak magnetic flux region outside the gap between the magnets and suppression of convection in the strong magnetic flux region inside the gap between the magnets. As the fringe-width increases, the magnetic field becomes weaker in the strong magnetic flux region but becomes stronger in the weak magnetic flux region. For large  $Ha_{z,max}$ , the increase of convection in the strong magnetic field region is unable to compensate for the suppression of convection in the weak magnetic flux region, resulting

in a decrease of the global heat and momentum transport with increasing fringe-width. However, for small  $Ha_{z,max}$ , the increase of convection in the strong magnetic field region is more than the decrease of convection in the weak magnetic flux region, resulting in an increase of global heat and momentum transport with increasing fringe-width.

We further analyzed wall-attached convection in the regions of strong magnetic flux. We showed that the amplitudes of the wall modes away from the corners decrease when  $\delta$  is decreased from 9 to 1, but begins to increase on further reduction of  $\delta$ . We believe that the horizontal components of the magnetic field play a crucial role in the stability of the wall modes. A detailed study on this behavior will be conducted in a future work.

Our present work provides important insights on the dynamics of thermal convection under spatially varying magnetic fields, which may find applications in several industrial and astrophysical flows. It should therefore be considered as a first step. For example, our results are expected to help in designing of engineering applications such as cooling blankets in fusion reactors. Although we worked on a small set of parameters, we expect our results to hold for higher Rayleigh numbers as well. In the future, we plan to conduct a similar analysis for fluids at different Prandtl numbers.

## Acknowledgements

The authors thank A. Pandey, Y. Kolesnikov, and M. Brynjell-Rahkola for useful discussions. The authors gratefully acknowledge the computing time provided to them on the high-performance computer Noctua2 at the NHR Center PC2. These are funded by the Federal Ministry of Education and Research and the state governments participating on the basis of the resolutions of the GWK for the national high performance computing at universities ([www.nhr-verein.de/unsere-partner](http://www.nhr-verein.de/unsere-partner)). The authors further acknowledge the Computing Center of Technische Universität Ilmenau for the resources provided to them for postprocessing and visualization of their simulation data.

## Funding

The work of S.B. is sponsored by a Postdoctoral Fellowship of the Alexander von Humboldt Foundation, Germany.

## Declaration of interests

The authors report no conflict of interest.

## Author ORCIDs

Shashwat Bhattacharya <https://orcid.org/0000-0001-7462-7680>  
 Thomas Boeck <https://orcid.org/0000-0002-0814-7432>  
 Dmitry Krasnov <https://orcid.org/0000-0002-8339-7749>  
 Jörg Schumacher <https://orcid.org/0000-0002-1359-4536>

## REFERENCES

AHLERS, G., GROSSMANN, S. & LOHSE, D. 2009 Heat transfer and large scale dynamics in turbulent Rayleigh-Bénard convection. *Rev. Mod. Phys.* **81** (2), 503–537.

AKHMEDAGAEV, R., ZIKANOV, O., KRASNOV, D. & SCHUMACHER, J. 2020a Rayleigh-Bénard convection in strong vertical magnetic field: flow structure and verification of numerical method. *Magnetohydrodynamics* **56**, 157–166.

AKHMEDAGAEV, R., ZIKANOV, O., KRASNOV, D. & SCHUMACHER, J. 2020b Turbulent Rayleigh-Bénard convection in a strong vertical magnetic field. *J. Fluid Mech.* **895**, R4.

AURNOU, J. M. & OLSON, P. L. 2001 Experiments on Rayleigh-Bénard convection, magnetoconvection and rotating magnetoconvection in liquid gallium. *J. Fluid Mech.* **430**, 283–307.

BHATTACHARYA, S., VERMA, M. K. & SAMTANEY, R. 2021 Revisiting Reynolds and Nusselt numbers in turbulent thermal convection. *Phys. Fluids* **33**, 015113.

BREUER, M., WESSLING, S., SCHMALZL, J. & HANSEN, U. 2004 Effect of inertia in Rayleigh-Bénard convection. *Phys. Rev. E* **69** (2), 026302.

BURR, U. & MÜLLER, U. 2001 Rayleigh-Bénard convection in liquid metal layers under the influence of a vertical magnetic field. *Phys. Fluids* **13**, 3247–3257.

BURR, U. & MÜLLER, U. 2002 Rayleigh-Bénard convection in liquid metal layers under the influence of a horizontal magnetic field. *J. Fluid Mech.* **453**, 345–369.

BUSSE, F. H. 2008 Asymptotic theory of wall-attached convection in a horizontal fluid layer with a vertical magnetic field. *Phys. Fluids* **20** (2), 024102.

BUSSE, F. H. & CLEVER, R. M. 1983 Stability of convection rolls in the presence of a horizontal magnetic field. *J. Theor. Appl. Mech.* **2**, 495–502.

CHANDRASEKHAR, S. 1981 *Hydrodynamic and Hydromagnetic Stability*. Oxford: Dover publications.

CHILLÀ, F. & SCHUMACHER, J. 2012 New perspectives in turbulent Rayleigh-Bénard convection. *Eur. Phys. J. E* **35** (7), 58.

CIONI, S., CHAUMAT, S. & SOMMERIA, J. 2000 Effect of a vertical magnetic field on turbulent Rayleigh-Bénard convection. *Phys. Rev. Lett.* **62** (4), R4520–R4523.

DAVIDSON, PETER A. 2017 *An Introduction to Magnetohydrodynamics*, 2nd edn. Cambridge: Cambridge University Press.

ECKE, R. E., ZHONG, F. & KNOBLOCH, E. 1992 Hopf bifurcation with broken reflection symmetry in rotating Rayleigh-Bénard convection. *Europhys. Lett.* **19**, 177–182.

FAUVE, S., LAROCHE, C. & LIBCHABER, A. 1981 Effect of a horizontal magnetic field on convective instabilities in mercury. *J. Physique Lett.* **42** (21), L455.

GOLDSTEIN, H. F., KNOBLOCH, E., MERCADER, I. & NET, M. 1993 Convection in a rotating cylinder. Part 1. Linear theory for moderate Prandtl numbers. *J. Fluid Mech.* **248**, 583–604.

GOLDSTEIN, H. F., KNOBLOCH, E., MERCADER, I. & NET, M. 1994 Convection in a rotating cylinder. Part 2. Linear theory for low Prandtl numbers. *J. Fluid Mech.* **262**, 293–324.

GRANNAN, A. M., CHENG, J. S., AGGARWAL, A., HAWKINS, E. K., XU, Y., HORN, S., SÁNCHEZ-ÁLVAREZ, J. & AURNOU, J. M. 2022 Experimental pub crawl from Rayleigh-Bénard to magnetostrophic convection. *J. Fluid Mech.* **939**, R1.

GRÖTZBACH, G. 1983 Spatial resolution requirements for direct numerical simulation of the Rayleigh-Bénard convection. *J. Comput. Phys.* **49** (2), 241–264.

HORN, S. & SCHMID, P. J. 2017 Prograde, retrograde, and oscillatory modes in rotating Rayleigh-Bénard convection. *J. Fluid Mech.* **831**, 182–211.

HOUCHENS, B. C., WITKOWSKI, L. MARTIN & WALKER, J. S. 2002 Rayleigh-bénard instability in a vertical cylinder with a vertical magnetic field. *J. Fluid Mech.* **469**, 189–207.

HURLBURT, N., MATTHEWS, P. & PROCTOR, M. 1996 Nonlinear compressible convection in oblique magnetic fields. *Ap. J.* **457**, 933.

KING, E. M. & AURNOU, J. M. 2015 Magnetostrophic balance as the optimal state for turbulent magnetoconvection. *Proc. Natl. Acad. Sci. U.S.A.* **112**, 990–994.

KING, E. M., STELLMACH, S. & AURNOU, J. M. 2012 Heat transfer by rapidly rotating Rayleigh-Bénard convection. *J. Fluid Mech.* **691**, 568–582.

KRASNOV, D., ZIKANOV, O. & BOECK, T. 2011 Comparative study of finite difference approaches in simulation of magnetohydrodynamic turbulence at low magnetic reynolds number. *Comput. Fluids* **50** (1), 46 – 59.

KRUG, D., LOHSE, D. & STEVENS, R. J. A. M. 2020 Coherence of temperature and velocity superstructures in turbulent Rayleigh-Bénard convection. *J. Fluid Mech.* **887**, A2.

LIU, W., KRASNOV, D. & SCHUMACHER, J. 2018 Wall modes in magnetoconvection at high Hartmann numbers. *J. Fluid Mech.* **849**, R2.

LIU, Y. & ECKE, R. E. 1999 Nonlinear travelling waves in rotating Rayleigh–Bénard convection: stability boundaries and phase diffusion. *Phys. Rev. E* **59**, 4091–4105.

NAKAGAWA, Y. 1957 Experiments on the inhibition of thermal convection by a magnetic field. *Proc. R. Soc. Lond.* **240**, 108–113.

NICOSKI, J. A., YAN, M. & CALKINS, M. A. 2022 Quasistatic magnetoconvection with a tilted magnetic field. *Phys. Rev. Fluids* **7**, 043504.

PANDEY, A., SCHEEL, J. D. & SCHUMACHER, J. 2018 Turbulent superstructures in Rayleigh–Bénard convection. *Nat. Commun.* **9**, 2118.

PEYRET, R. 2002 *Spectral Methods for Incompressible Viscous Flows*. New York: Springer.

ROBERTS, P. H. 1967 *An introduction to magnetohydrodynamics*. London: Longmans.

SCHEEL, J. D., KIM, E. & WHITE, K. R. 2012 Thermal and viscous boundary layers in turbulent Rayleigh–Bénard convection. *J. Fluid Mech.* **711**, 281–305.

SCHUMACHER, J. 2022 The various facets of liquid metal convection. *J. Fluid Mech.* **946**, F1.

SCHUMACHER, JÖRG & SREENIVASAN, KATEPALLI R. 2020 Colloquium: Unusual dynamics of convection in the Sun. *Rev. Mod. Phys.* **92**, 041001.

STEVENS, RICHARD J. A. M., BLASS, ALEXANDER, ZHU, XIAOJUE, VERZICCO, ROBERTO & LOHSE, DETLEF 2018 Turbulent thermal superstructures in Rayleigh–Bénard convection. *Phys. Rev. Fluids* **3**, 041501(R).

TASAKA, Y., IGAKI, K., YANAGISAWA, T., VOGT, T., ZÜRNER, T. & ECKERT, S. 2016 Regular flow reversals in Rayleigh–Bénard convection in a horizontal magnetic field. *Phys. Rev. E* **93**, 043109.

VERMA, M. K. 2018 *Physics of Buoyant Flows: From Instabilities to Turbulence*. Singapore: World Scientific.

VERMA, M. K. 2019 *Energy transfers in Fluid Flows: Multiscale and Spectral Perspectives*. Cambridge: Cambridge University Press.

VERZICCO, R. & CAMUSSI, R. 2003 Numerical experiments on strongly turbulent thermal convection in a slender cylindrical cell. *J. Fluid Mech.* **477**, 19–49.

VOGT, T., ISHIMI, W., YANAGISAWA, T., TASAKA, Y., SAKURABA, A. & ECKERT, S. 2018 Transition between quasi-two-dimensional and three-dimensional Rayleigh–Bénard convection in a horizontal magnetic field. *Phys. Rev. Fluids* **3**, 013503.

VOGT, T., YANG, J.-C., SCHINDLER, F. & ECKERT, S. 2021 Free-fall velocities and heat transport enhancement in liquid metal magneto-convection. *J. Fluid Mech.* **915**, A68.

VOTYAKOV, E. V., KASSINOS, S. C. & ALBETS-CHICO, X. 2009 Analytic models of heterogenous magnetic fields for liquid metal flow simulations. *Theor. Comput. Fluid. Dyn.* **23**, 571–578.

WEISS, N. O. & PROCTOR, M. R. E. 2014 *Magnetoconvection*. Cambridge: Cambridge University Press.

YAN, M., CALKINS, M., MAFFEI, A., JULIEN, K., TOBIAS, S. & MARTI, P. 2019 Heat transfer and flow regimes in quasi-static magnetoconvection with a vertical magnetic field. *J. Fluid Mech.* **877**, 1186–1206.

YANAGISAWA, T., HAMANO, Y., MIYAGOSHI, T., YAMAGISHI, Y., TASAKA, Y. & TAKEDA, Y. 2013 Convection patterns in a liquid metal under an imposed horizontal magnetic field. *Phys. Rev. E* **88** (6), 063020.

ZHANG, X., VAN GILS, D. P. M., HORN, S., WEDI, M., ZWIRNER, L., AHLERS, G., ECKE, R. E., WEISS, S., BODENSCHATZ, E. & SHISHKINA, O. 2020 Boundary Zonal Flow in Rotating Turbulent Rayleigh–Bénard Convection. *Phys. Rev. Letters* **124**, 084505.

ZHONG, F., ECKE, R. E. & STEINBERG, V. 1991 Asymmetric modes and transition to vortex structures in rotating Rayleigh–Bénard convection. *Phys. Rev. Lett.* **67**, 2473–2476.

ZIKANOV, O. & THESS, A. 1998 Direct numerical simulation of forced MHD turbulence at low magnetic Reynolds number. *J. Fluid Mech.* **358**, 299–333.

ZÜRNER, T., SCHINDLER, F., VOGT, T., ECKERT, S. & SCHUMACHER, J. 2020 Flow regimes of Rayleigh–Bénard convection in a vertical magnetic field. *J. Fluid Mech.* **894**, A21.